Robust Real-Time Thrust Fault Diagnosis for UAVs: A Physics-Informed Framework Decoupling Wind Disturbances

Taegyun Kim[1] and Seungkeun Kim[1,2]

[1] *Department of Research and Development. Unlabel Inc, Daejeon, 34134, Republic of Korea*
ktg92@cnu.ac.kr

[2] *Department of Aerospace Engineering, Chungnam National University, Daejeon, 34134, Republic of Korea*
skim78@cnu.ac.kr

ABSTRACT

Operational reliability of multi-rotor Unmanned Aerial Vehicles (UAVs) is frequently compromised by the ambiguity between external wind disturbances and internal thrust faults. This paper proposes a physics-informed fault diagnosis (PI-FDI) framework that explicitly decouples wind-induced effects from total observed disturbances. By integrating an Extended Kalman Filter (EKF) for real-time wind estimation and a Disturbance Observer (DOB) for total torque monitoring, the framework isolates a clean fault residual through physical coefficient mapping. High-fidelity 6-DOF simulations involving Dryden turbulence and non-stationary discrete gusts demonstrate a rapid detection latency of 0.18 s for a 20% thrust loss, maintaining near-zero false alarms even during peak gust periods. Furthermore, a 300-trial Monte Carlo simulation confirmed high fault isolation accuracy, demonstrating superior statistical robustness across varying wind intensities and randomized fault modes. The proposed physics-informed decoupling approach significantly enhances diagnostic resilience, providing a critical foundation for real-time fault-tolerant control in mission-critical UAV operations.

1. INTRODUCTION

The rapid proliferation of multi-rotor Unmanned Aerial Vehicles (UAVs) in mission-critical operations, such as disaster response and infrastructure inspection, has intensified the demand for high-reliability Fault Detection and Isolation (FDI) systems. In these applications, the ability to maintain flight stability despite internal component faults is paramount. However, UAVs are inherently sensitive to environmental disturbances, particularly wind gusts and turbulence, which often manifest as sensor signatures strikingly similar to those of thrust degradations.

A major challenge in current FDI research is the ambiguity between external aerodynamic effects and internal thrust faults. In unpredictable and dynamic environments, integrating condition information is crucial for maintaining overall system availability (Dingeldein, 2024). While data-driven approaches using deep learning have shown promise in fault classification (Kim, Jeong, & Kim, 2024), they typically require extensive datasets and lack the transparency necessary for safety-critical certification.

Furthermore, model-based observers, such as the standard Disturbance Observer (DOB), have been widely adopted for flight stability (Guo, Jia, Yu, Guo, & Xie, 2020); (Jeong, Suk, & Kim, 2024). However, these conventional structures often treat all deviations as a lumped disturbance, making it extremely difficult to isolate the pure fault component from environmental noise. This lumped approach limits diagnostic accuracy in unpredictable weather, necessitating a more sophisticated separation strategy for fault-tolerant control (Du, Huang, Cheng, Fan, & Yuan, 2023);(Lee et al., 2026).

To address these limitations, this paper proposes a Physics-Informed FDI (PI-FDI) framework that explicitly decouples wind-induced moments from the total observed disturbance. Building upon foundational geometric decoupling and observer concepts (Kim et al., 2024), the core innovation lies in the synergy between an Extended Kalman Filter (EKF) for real-time wind estimation and a DOB for total torque observation. By mapping the estimated wind velocity to aerodynamic moments using known physical coefficients, the framework isolates the fault residual. This decoupling process ensures that the diagnostic logic remains sensitive to minor thrust faults while staying robust against wind gusts.

It is worth clarifying the scope of this novelty. Both the EKF for wind estimation and the DOB for disturbance observation are individually well-established tools, and a range of fault-tolerant control schemes—including two-stage Kalman filtering (Zhao et al., 2025), adaptive backstepping sliding-mode

control (Nguyen et al., 2024), nonsingular terminal sliding-mode control (Liu et al., 2020), incremental sliding-mode allocation (Wang et al., 2021), and robust backstepping attitude control (Ben et al., 2022)—have been proposed to cope with actuator faults and disturbances. Rather than competing with these controllers, the contribution here is the explicit combination-and-subtraction scheme that maps the EKF wind estimate into the moment space and removes it from the DOB output, yielding a fault residual that is, by construction, decoupled from wind.

The main contributions of this paper are as follows:

1. Development of a physics-informed decoupling architecture that effectively distinguishes between environmental noise and thrust faults;
2. Achievement of low-latency fault detection suitable for real-time fault-tolerant control systems;
3. Statistical validation of fault isolation reliability through extensive Monte Carlo simulations under stochastic wind conditions.

The remainder of this paper is organized as follows. Section 2 describes the proposed PI-FDI framework and its mathematical formulation. Section 3 outlines the numerical simulation environment and scenario settings. Section 4 presents the results and discussion based on both transient and stochastic analyses. Finally, Section 5 concludes the paper and discusses future research directions.

2. PHYSICS-INFORMED FDI FRAMEWORK

The proposed framework is designed to resolve the ambiguity between external wind disturbances and internal thrust faults in multi-rotor UAVs. The system employs a disturbance-decoupling architecture consisting of three primary stages: wind estimation, signal decoupling, and fault identification. The overall diagnostic procedure is visualized in Fig.1, depicting how the EKF-based wind estimation and DOB-based total disturbance observation are synergized to isolate the pure fault signal.

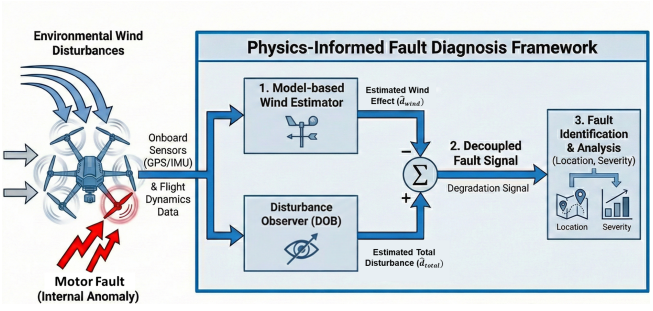

Figure 1. Overall architecture of the proposed physics-informed fault diagnosis framework

By explicitly mapping the physical relationships between wind velocity and aerodynamic moments, the framework ensures that environmental factors do not contaminate the diagnostic.

2.1. Wind Estimation

The first stage of the proposed framework involves estimating the environmental wind velocity vector using the EKF. Unlike conventional methods that require specialized anemometers, this approach utilizes the UAV's acceleration responses as an indirect measure of wind influence (Zyadat, Horri, Innocente, & Statheros, 2023).

The EKF is designed with a state vector $\mathbf{x}_{ekf} = [v_{w,x}, v_{w,y}]^T$, representing the horizontal wind velocity components in the Earth-fixed frame. The state transition model assumes a random walk process to account for the stochastic nature of wind turbulence. The measurement model is formulated based on the UAV's translational dynamics, where the horizontal accelerations (a_x, a_y) measured by the IMU serve as the observation vector $\mathbf{z}_m$:

$$\mathbf{z}_m = \mathbf{a}_{thrust,xy} - \frac{C_{drag}}{m}(\mathbf{v}_{xy} - \mathbf{x}_{ekf}) + \mathbf{v}_{noise} \tag{1}$$

where $\mathbf{a}_{thrust,xy}$ is the acceleration contributed by the motor thrust, $\mathbf{v}_{xy}$ is the UAV's ground velocity, and C_{drag} is the aerodynamic drag coefficient. By linearizing this relationship, the EKF recursively updates the wind velocity estimate, effectively filtering out high-frequency sensor noise and structural vibrations. Here, C_{drag} is assumed isotropic, i.e., independent of the wind direction, so that the same scalar coefficient applies to both horizontal axes.

Finally, the estimated wind velocity vector is mapped to the resulting aerodynamic moments. To provide a clear physical representation of this mapping, the relationship is expanded into its component-wise form as follows:

$$\begin{bmatrix} \hat{d}_{wind,roll} \\ \hat{d}_{wind,pitch} \\ \hat{d}_{wind,yaw} \end{bmatrix} = \begin{bmatrix} v_{w,x} \\ v_{w,y} \\ v_{w,z} \end{bmatrix} \odot \begin{bmatrix} C_{moment,x} \\ C_{moment,y} \\ C_{moment,z} \end{bmatrix} = \begin{bmatrix} v_{w,x} \cdot C_{moment,x} \\ v_{w,y} \cdot C_{moment,y} \\ v_{w,z} \cdot C_{moment,z} \end{bmatrix} \tag{2}$$

where $\hat{d}_{wind}$ is the estimated aerodynamic moment vector, $\hat{v}_w$ is the estimated wind velocity vector, C_{moment} is the predefined aerodynamic moment coefficient vector, and $\odot$ denotes the Hadamard (element-wise) product. Since the EKF state contains only the two horizontal components, the vertical wind component is assumed negligible ($v_{w,z} = 0$); accordingly, the yaw-axis wind moment $\hat{d}_{wind,yaw}$ vanishes in the present formulation.

2.2. Total Disturbance Estimation via DOB

To estimate the total lumped disturbance acting on the airframe, the DOB is implemented in the rotational dynamics. The DOB considers all external torques, including wind-induced

moments and thrust faults, as a lumped disturbance (Jing, Mirza, Sipahi, & Martinez-Lorenzo, 2023). The observer structure is formulated based on the nominal plant inverse and a low-pass filter $Q(s)$:

$$\hat{\mathbf{d}}_{total}(s) = Q(s)\left[\mathbf{J}_n\dot{\omega}(s) - \mathbf{u}_m(s)\right] \tag{3}$$

where $\hat{\mathbf{d}}_{total}(s)$ is the lumped disturbance including wind-induced moments and thrust faults, $Q(s)$ is the low-pass filter, $\mathbf{J}_n$ denotes the nominal inertia matrix, $\dot{\omega}(s)$ is the measured angular acceleration, and $u_m(s)$ is the torque command.

2.3. Fault Identification and Isolation Logic

The decoupled fault signal $\hat{d}_{fault}$ is isolated by subtracting the estimated wind from the total disturbance as follows:

$$\hat{d}_{fault} \approx \hat{d}_{total} - \hat{d}_{wind} \tag{4}$$

This signal is further processed to identify the specific faulty thrust. The isolation logic relies on the mixer (control allocation) matrix $\mathbf{M}$ of size 3×6, which maps the six individual motor thrusts $\mathbf{f} = [f_1, \ldots, f_6]^T$ to the body-frame roll, pitch, and yaw moments through $\boldsymbol{\tau} = \mathbf{M}\mathbf{f}$. For the hexacopter geometry, the i-th column $\mathbf{m}_i$ of this matrix is defined as

$$\mathbf{m}_i = \begin{bmatrix} -L\sin\beta_i \\ L\cos\beta_i \\ \sigma_i\, k_{drag}/k_{thrust} \end{bmatrix}, \qquad \beta_i = (i-1)\frac{\pi}{3} \tag{5}$$

where L is the arm length, β_i is the azimuth angle of the i-th motor (evenly spaced by $60°$), and $\sigma_i \in \{+1, -1\}$ denotes its rotation direction (CW/CCW). Because a thrust loss in motor i reduces its force, the associated fault moment acts along $-\mathbf{m}_i$. An isolation score S_i for the i-th motor is therefore obtained by measuring the directional similarity between the residual and $-\mathbf{m}_i$:

$$S_i = \frac{\hat{d}_{fault}^T \cdot (-\mathbf{m}_i)}{\|\hat{d}_{fault}\| \cdot \|\mathbf{m}_i\|} \tag{6}$$

The system identifies the motor with the highest similarity score ($S_i \approx 1$) as the faulty component (Cao, Yang, Wang, Liu, & Hu, 2022). In addition to location, the fault severity is estimated by comparing the magnitude of the decoupled residual against the nominal thrust contribution as follows:

$$\Delta f \approx \frac{||\hat{d}_{fault}||}{||\mathbf{m}_{target}||} \tag{7}$$

where Δf is the estimated fault severity, and $\mathbf{m}_{target}$ is the thrust contribution vector of the identified faulty motor.

3. NUMERICAL SIMULATION SETUP

3.1. Hexacopter Model Parameters

The plant model is based on a standard hexacopter UAV configuration, as illustrated in Fig.2 To replicate realistic flight conditions, a 10% model uncertainty was introduced between the true inertia (J_{true}) and the nominal inertia (J_n) used in the observer design (Shim, Park, Joo, Back, & Jo, 2016). The specific physical parameters used in the simulation are summarized in Tab. 1. The vehicle dynamics are propagated as a full 6-DOF rigid-body model integrated with a fixed-step fourth-order Runge–Kutta scheme at the sampling time dt. The physical parameters in Tab. 1 were chosen to represent a typical 2 kg-class hexacopter, with the inertia and arm length consistent with our previous experimental platform (Kim et al., 2024).

Table 1. Physical parameters of the hexacopter UAV

Parameter	Value	Unit
Mass (m)	2.0	kg
Arm length (L)	0.25	m
Inertia (J_x, J_y)	0.02	kg·m^2
Inertia (J_z)	0.04	kg·m^2
Thrust coeff. (k_{thrust})	1.0×10^{-5}	N·s^2
Drag coeff. (k_{drag})	1.0×10^{-6}	N·m·s^2
Aerodynamic drag (C_{drag})	0.5	-
Roll, Pitch moment coeff. ($C_{moment,x,y}$)	0.1	N·s
Yaw moment coeff. ($C_{moment,z}$)	0.05	N·s

3.2. Environmental Wind Conditions

The environmental disturbances are modeled by combining Dryden turbulence and discrete wind gusts to replicate complex aerodynamics (Langelaan, Alley, & Neidhoefer, 2011). The Dryden turbulence model generates stochastic wind velocity components based on a mean reference wind speed of

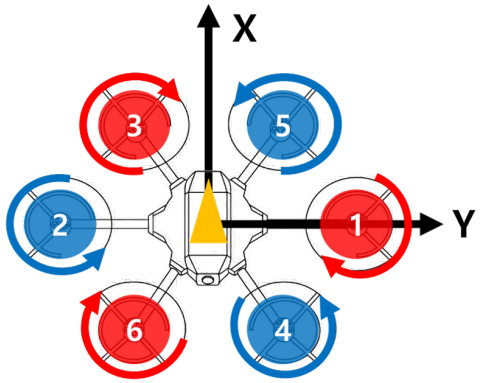

Figure 2. Schematic of the hexacopter UAV configuration with motor numbering and rotation directions.

$V_w = 10$ m/s. The gust velocity, V_{gust}, is defined as follows:

$$V_{gust}(t) = \frac{V_m}{2}\left[1 - \cos\left(\frac{2\pi(t - t_{start})}{d_g}\right)\right] \quad (8)$$

where V_m is the magnitude of the gust, t_{start} is the activation time of the gust, and d_g is the duration of the gust.

3.3. Fault Injection and Environmental Scenarios

Two distinct validation cases are established to evaluate real-time decoupling and statistical reliability.

Case 1: Dynamic Disturbance Decoupling
This case demonstrates the FDI's ability to distinguish between environmental factors and internal anomalies through a four-phase sequence:

1. **P1: Baseline** ($0 \leq t < 5$ **s**): Normal flight under background Dryden turbulence.
2. **P2: Gust-only** ($5 \leq t < 10$ **s**): Strong discrete wind gust is applied without any fault to verify the false alarm suppression capability.
3. **P3: Combined** ($10 \leq t < 15$ **s**): A 20% thrust loss ($\Delta f = 0.2$) is injected into Motor 1 at $t = 10$ s, coinciding with the peak of the wind gust, to evaluate decoupling performance.
4. **P4: Fault-only** ($t \geq 15$ **s**): Evaluation of diagnostic stability after the gust has dissipated.

Case 2: Statistical Reliability via Monte Carlo Simulation
A Monte Carlo simulation consisting of 300 independent trials is conducted to validate generalized consistency. In this case, wind speed (V_w), faulty motor ID, and fault severity (Δf) are randomized, with Δf sampled from a uniform distribution between 5% and 40%.

4. RESULTS AND DISCUSSION

In this section, the diagnostic performance of the proposed physics-informed framework is evaluated based on the two simulation cases defined in Section 3.3.

4.1. Real-Time Decoupling and Detection Performance

The simulation results of Case 1 are presented in Fig.3.

During the **P2: Gust-only** period ($5 \leq t < 10$ s), the hexacopter is subjected to significant aerodynamic moments reaching approximately 0.8 Nm, as shown in Fig.3(a) and 3(d). While the total disturbance estimated by the DOB fluctuates heavily, the EKF-based wind estimator effectively tracks these environmental components. Consequently, the decoupled fault residuals in Fig.3 (c) and 3(f) remain within a near-zero bound (< 0.2 Nm), demonstrating that the framework successfully prevents false alarms under harsh wind conditions.

Upon injecting a 20% thrust loss into Motor 1 at $t = 10$ s (**P3: Combined**), the residual signal in the roll axis immediately deviates from the baseline. The framework detected the anomaly at $t = 10.18$ s, resulting in a detection latency of 0.18 s. Despite the ongoing peak wind disturbances, the isolated signal clearly reflects the pure fault magnitude. In the final phase (**P4: Fault-only**), the decoupled residual maintains a stable value corresponding to the actual fault severity even after the gust dissipates.

To address whether a simpler detector would suffice, Tab. 2 compares the proposed framework against a naïve baseline: a fixed-threshold (step) detector applied directly to the raw, non-decoupled DOB residual, which lumps the wind and the fault into a single signal. Although Fig. 3(c) and (f) display a clear time-scale separation between the abrupt fault and the surrounding dynamics, this separation is a property of the *decoupled* residual rather than of the raw signal. In Fig. 3(a) and (d), the gust alone drives the raw residual up to about 0.8 Nm—far larger than the moment perturbation caused by the 20% thrust loss—so any threshold low enough to flag the fault is already exceeded during the gust. The naïve detector therefore raises a false alarm in the wind-only phase (P2) and cannot report a meaningful detection latency. In contrast, the proposed PI-FDI keeps the residual below 0.2 Nm under the same gust, detects the fault within 0.18 s, and sustains an isolation accuracy above 99% across the 300 Monte Carlo trials, which justifies the decoupling step.

Table 2. Comparative summary of diagnostic performance metrics between standard DOB and proposed PI-FDI.

Performance Metric	Standard DOB	Proposed PI-FDI
Max Residual (Wind-only)	0.8 Nm	0.2 Nm
Detection Latency ($\Delta f = 0.2$)	N/A (False Alarm)	**0.18 s**
Isolation Accuracy (300 trials)	Low (Ambiguity)	**>99%**

4.2. Analysis of Flight Stability and Dynamic Response

To evaluate the impact of the proposed FDI framework on operational stability, the attitude response and body angular rates for Case 1 were analyzed, as shown in Fig. 4.

During the P2 and P3, the hexacopter exhibits noticeable oscillations in roll and pitch angles due to the discrete gusts. However, the attitude remains within a stable bound of ± 0.6 degrees throughout the simulation. At $t = 10$ s, the injection of a 20% thrust loss induces a transient spike in the roll rate (p), reaching approximately 7.5 deg/s. The onboard controller successfully rejects this perturbation within 0.5 s, restoring the angular rates to their baseline turbulence levels.

This stable regulation confirms that the diagnostic process operates effectively during active flight without compromising vehicle safety. Furthermore, the 3D stroboscopic trajectory in Fig. 5 illustrates that the UAV maintains its mission profile without critical altitude loss, demonstrating the framework's robustness during complex transitions between environmen-

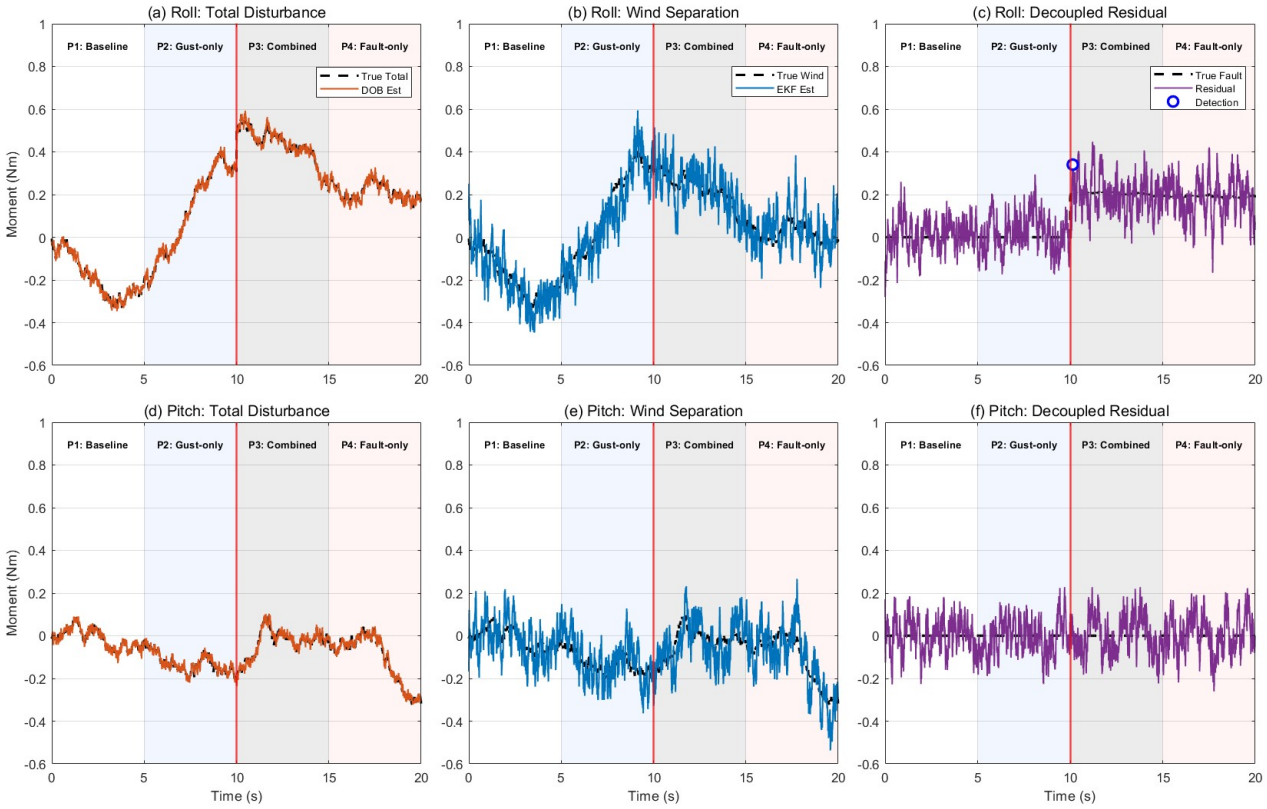

Figure 3. Time-domain simulation results for Case 1: (a, d) Total disturbance estimation by DOB, (b, e) wind-induced moment separation via EKF, and (c, f) isolated fault residual $\hat{d}_{fault}$. Shaded regions distinguish the four phases (P1-P4). The vertical red line marks the $t = 10$ s thrust-fault injection.

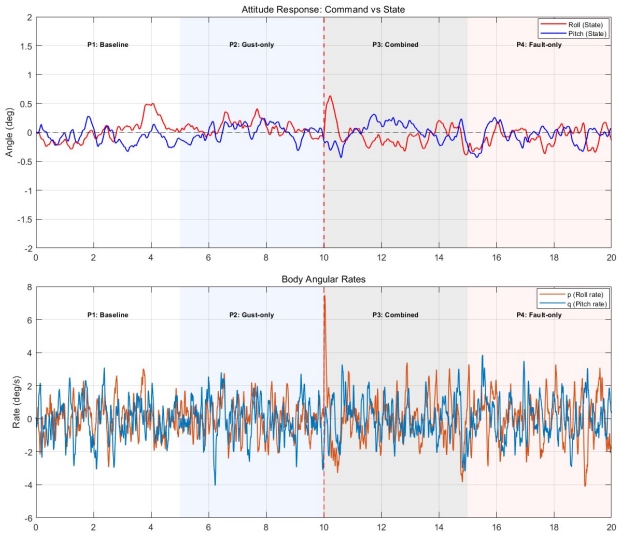

Figure 4. Flight performance under combined disturbances

tal disturbances and thrust degradation.

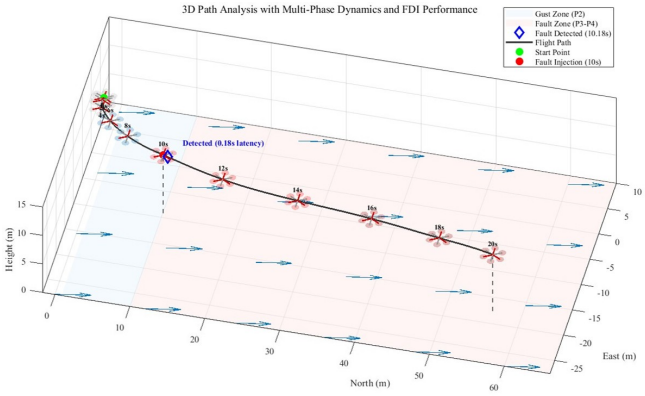

Figure 5. 3D trajectory analysis with global wind field. The markers and drop lines illustrate the vehicle's attitude and 0.18 s detection latency under environmental disturbances.

4.3. Statistical Reliability and Fault Isolation

To verify the generalized consistency, Case 2 was analyzed using 300 independent trials. As illustrated in Figure 6, the

decoupled residuals form six distinct directional clusters, each corresponding to the specific torque contribution of the faulty motor defined by the hexacopter's geometry. Faults in Motor

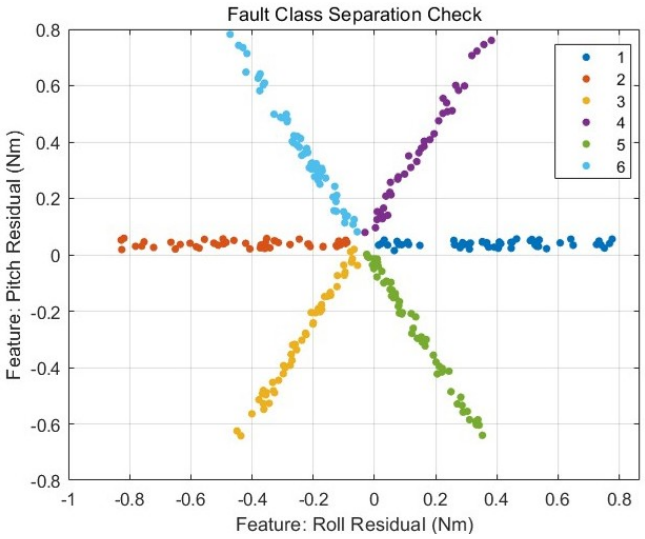

Figure 6. Fault class separation check via 300-trial Monte Carlo simulations. Each point is a decoupled residual projected onto the roll- and pitch-moment axes; the six clusters correspond to the six motors, with their angular positions matching each motor's column $-\mathbf{m}_i$ of the mixer matrix.

1 and Motor 2 align with the roll axis, while the diagonal motors (3, 4, 5, and 6) exhibit combined roll and pitch signatures. Notably, the residuals for each motor maintain a high degree of linearity and directional consistency despite the stochastic nature of the turbulence and randomized fault severities.

4.4. Discussion on Diagnostic Robustness and Limitations

While the 300-trial Monte Carlo simulation yielded an exceptional isolation accuracy, this result should be interpreted within the context of the controlled numerical environment. The high reliability is primarily attributed to the geometric decoupling logic, which leverages the distinct torque signatures of the hexacopter's motor configuration. Physically, because each motor occupies a distinct position and spin direction, a fault in a given motor drives the residual moment vector along a unique direction—namely its own column $-\mathbf{m}_i$ of the mixer matrix in Eq. (5). The isolation logic thus identifies the faulty motor by checking which of these six fixed directions the decoupled residual best aligns with. However, certain edge cases may pose challenges to the framework's robustness. For instance, when the fault severity is extremely low or when the sensor noise level exceeds the diagnostic threshold, the residual vector may exhibit directional ambiguity, potentially leading to misidentification among spatially adjacent motors. Furthermore, unmodeled aerodynamic effects, such as the ground effect during takeoff or rapid maneuvering, could introduce non-stationary biases that are not fully captured by the current EKF-based wind estimator. More broadly, the present study is confined to simulation, and the dominant sim-to-real gap stems from two sources. First, only a single fault mode (partial thrust loss) is modeled, whereas real motors also exhibit complete failures and bias-type faults. Second, several noise sources—airframe vibration, sensor bias, and unmodeled aerodynamics—are not represented in the current model. A dedicated experimental quantification of these effects is left to future work.

5. CONCLUSION

This paper presented a robust physics-informed fault diagnosis framework for multi-rotor UAVs, specifically designed to decouple environmental wind disturbances from internal thrust faults. By synergizing an EKF-based wind estimator with the DOB, the proposed architecture isolates a clean fault residual, effectively suppressing false alarms induced by aerodynamic moments.

The framework's performance was validated through comprehensive 6-DOF simulations. The time-domain analysis demonstrated a rapid detection latency of 0.18s following a 20% thrust loss, even under peak discrete gusts and Dryden turbulence. Furthermore, the 300-trial Monte Carlo simulation confirmed a high isolation accuracy, with decoupled residuals forming geometrically consistent clusters. Future research will focus on the experimental validation of this framework using actual flight test data and its integration with fault-tolerant control to ensure autonomous system resilience.

ACKNOWLEDGMENT

This research was supported by Unmanned Vehicles Core Technology Research and Development Program through the National Research Foundation of Korea (NRF) and Unmanned Vehicle Advanced Research Center (UVARC) funded by the Ministry of Science and ICT, the Republic of Korea (2020M3C1C1A01083162).

NOMENCLATURE

C_{drag}	Aerodynamic drag coefficient
d_g	Duration of the discrete wind gust
dt	Simulation sampling time step
m	Total mass of the UAV
p, q, r	Body angular rates (roll, pitch, yaw)
t_{start}	Activation time of the wind gust
V_m	Magnitude of the discrete wind gust
V_w	Reference wind velocity (Dryden model)
x, y, z	Vehicle position in the NED frame
ϕ, θ, ψ	Euler angles (roll, pitch, yaw)
ω	Angular velocity vector
$\hat{d}$	Estimated disturbance torque from DOB
τ_f	Residual torque associated with thrust fault

REFERENCES

Ben, A., et al. (2022). New robust backstepping attitude control approach applied to quanser 3 dof hover quadrotor in the case of actuators faults. *Nonlinear Dynamics*, *108*(3), 2145-2160.

Cao, L., Yang, X., Wang, G., Liu, Y., & Hu, Y. (2022). Fault detection based on extended state observer and interval observer for uavs. *Aircraft Engineering and Aerospace Technology*, *94*(10), 1759–1771.

Dingeldein, L. (2024). Integration of condition information in uav swarm management to increase system availability in dynamic environments. In *8th european conference of the prognostics and health management society* (p. 565-575).

Du, Y., Huang, P., Cheng, Y., Fan, Y., & Yuan, Y. (2023). Fault tolerant control of a quadrotor unmanned aerial vehicle based on active disturbance rejection control and two-stage kalman filter. *IEEE Access*, *11*(1), 67556-67566.

Guo, K., Jia, J., Yu, X., Guo, L., & Xie, L. (2020). Multiple observers based anti-disturbance control for a quadrotor uav against payload and wind disturbances. *Control Engineering Practice*, *102*, 104560.

Jeong, H., Suk, J., & Kim, S. (2024). Control of quadrotor uav using variable disturbance observer-based strategy. *Control Engineering Practice*, *150*, 105990.

Jing, Y., Mirza, A., Sipahi, R., & Martinez-Lorenzo, J. (2023). Sliding mode controller with disturbance observer for quadcopters; experiments with dynamic disturbances and in turbulent indoor space. *Drones*, *7*(5), 328.

Kim, T., Jeong, H., & Kim, S. (2024). Thrust-fault diagnosis of hexacopter uav using supervised learning with disturbance observers. *International Journal of Control, Automation, and Systems*, *22*(12), 3584-3594.

Langelaan, J. W., Alley, N., & Neidhoefer, J. (2011). Wind field estimation for small unmanned aerial vehicles. *Journal of Guidance, Control, and Dynamics*, *34*(4), 1016-1030.

Lee, J. D., Kim, Y., Kim, Y., Lee, H., Cha, J.-H., & Bang, H. (2026). Sensor and actuator fault detection and isolation for urban air mobility. *IEEE Sensors Journal*.

Liu, X., et al. (2020). Nonsingular terminal sliding mode control for a quadrotor uav with a total rotor failure. *Journal of the Franklin Institute*, *357*(15), 10532-10550.

Nguyen, N., et al. (2024). Adaptive backstepping sliding mode fault-tolerant control of quadrotor uav in the presence of external disturbances, uncertainties, and simultaneous actuator and sensor faults. *International Journal of Computers Communications & Control*, *19*(1), 7018.

Shim, H., Park, G., Joo, Y., Back, J., & Jo, N. H. (2016). Yet another tutorial of disturbance observer: robust stabilization and recovery of nominal performance. *Control Theory and Technology*, *14*(3), 237-249.

Wang, B., et al. (2021). Incremental sliding-mode fault-tolerant flight control. *AIAA Journal of Guidance, Control, and Dynamics*, *44*(10), 1870-1882.

Zhao, L., et al. (2025). Experimental test of a two-stage kalman filter for actuator fault detection and diagnosis of an unmanned quadrotor helicopter. *IEEE Transactions on Control Systems Technology*, *34*(2), 550-562.

Zyadat, Z., Horri, N., Innocente, M., & Statheros, T. (2023). Observer-based optimal control of a quadplane with active wind disturbance and actuator fault rejection. *Sensors*, *23*(4), 1954.

BIOGRAPHIES

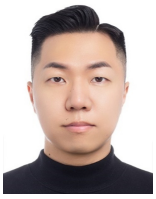

Taegyun Kim received his B.S., M.S., and Ph.D. degrees in aerospace engineering from Chungnam National University(CNU), Republic of Korea, in 2017, 2019, and 2024, respectively. He was a postdoctoral researcher at the Department of Aerospace Engineering, CNU, from 2024 to 2025. He is currently with the Department of Research and Development, Unlabel Inc., Republic of Korea. His current research interests include fault diagnosis, fault-tolerant control, EKF, and LLM.

Seungkeun Kim received his B.Sc. degree in mechanical and aerospace engineering from Seoul National University(SNU), Seoul, Korea, in 2002, and then acquired a Ph.D. degree from SNU in 2008. He is currently a professor at the Department of Aerospace Engineering, Chungnam National University, Korea. He was an associate professor and an assistant professor at the same university from 2012 to 2020. He was a visiting scholar at George Washington University at Washington D.C. in 2019. Previously, he was a research fellow and a lecturer at Cranfield University, United Kingdom from 2008 to 2012. His research interests include fault diagnosis, fault tolerant control, aircraft guidance and control, and estimation.